Dynamic Model of AC–AC Dual Active Bridge Converter Using the Extended Generalized Average Modeling Framework

Kartikeya Jayadurga Prasad Veeramraju, *Graduate Student Member, IEEE*, and Jonathan W. Kimball, *Senior Member, IEEE*

***Abstract*—The ac–ac dual active bridge (DAB) converter is an advanced bidirectional two-port grid interface converter that facilitates active and reactive power flow control between two grids without a dc-link capacitor. This article presents a novel modeling approach for the ac–ac DAB converter using the extended generalized average modeling (EGAM) technique. Unlike the conventional generalized average modeling (GAM) framework, the ac–ac DAB converter's dynamic state variables, including the leakage inductor current and ac grid side *LC filters*, exhibit grid and switching frequency components, making the standard GAM framework unsuitable for dynamic modeling involving two distinct excitation frequencies. Furthermore, the 2-D GAM (2D-GAM) framework, although capable of capturing the dynamics of two frequencies and their cross interactions, fails to handle product terms involving double fourier series (DFS) states resulting from the switching terms in the ac-ac DAB converter. To address these challenges, the EGAM technique is proposed, which involves transforming the DFS product terms in the time domain into the 2D-convolution of their discrete fourier images (DFI) in the frequency domain. As a consequence of this analysis, it is shown that in an ac–ac DAB converter, the power is transferred in the grid-switching sideband frequency components at the bridge level. The effectiveness of the EGAM modeling framework is demonstrated through extensive simulation and hardware experiments, and the results are compared with PLECS results, validating the accuracy and efficacy of the proposed approach.**

***Index Terms*—Dual active bridge (DAB) converter, dynamic phasor modeling, generalized averaged models, inverters, multifrequency averaging, power electronic converters, solid-state transformers (SST).**

NOMENCLATURE

$x(t)$	Time domain signal.
$\mathbf{C}(t)$	Basis function vector.
$\mathbf{x}_f$	Fourier coefficient vector.
$\mathbf{T}$	Frequency information matrix.
ω_ζ	First angular excitation frequency.
ω_χ	Second angular excitation frequency.
$q_+(t)$	Phase shift modulation switching function.
ϕ	DAB phase shift angle.
p	DFI first excitation axis control index.
r	DFI second excitation axis control index.
O	Total number of distinct frequencies.
L_1, L_2	Primary and secondary input ac link inductor.
C_1, C_2	Primary and secondary input ac link capacitor.
R_{L_1}, R_{L_2}	AC inductor resistance.
R_t	Transformer inductor resistance.
L_{lk}	Transformer leakage inductor.
i_{L_1}, i_{L_2}	Primary and secondary input ac link inductor currents.
$i_{L_{lk}}$	Transformer leakage inductor current.
v_{C_1}, v_{C_2}	Primary and secondary input ac link capacitance voltages.
v_i, v_o	Primary and secondary input ac voltages.
θ, δ	Primary and secondary input ac voltage phase angle.
Γ, Λ	Primary and secondary side voltage excitation vector.
Υ	Ancillary switching sparse vector.

Manuscript received 7 August 2023; revised 9 November 2023; accepted 7 December 2023. Date of publication 21 December 2023; date of current version 26 January 2024. This work was supported by the US Department of Energy, Energy Storage Program. Recommended for publication by Associate Editor J. He. *(Corresponding author: Jonathan W. Kimball.)*

Kartikeya Jayadurga Prasad Veeramraju is with Lunar Energy, Mountain View, CA 94043 USA (e-mail: kveeramraju@lunarenergy.com).

Jonathan W. Kimball is with the Department of Electrical and Computer Engineering, Missouri University of Science and Technology, Rolla, MO 65401 USA (e-mail: kimballjw@mst.edu).

Color versions of one or more figures in this article are available at https://doi.org/10.1109/TPEL.2023.3344378.

Digital Object Identifier 10.1109/TPEL.2023.3344378

I. INTRODUCTION

SOLID state transformers (SST) are becoming prevalent as the stability and power requirements for power distribution systems increase [1]. For the distribution level, reliable and straightforward circuit topologies are desired. A comprehensive review of the design challenges of SST can be found in [1], [2], [3], and [4]. SSTs of the first category [3], [5], [6], [7], [8], [9], [10] are generally simpler in construction and interface two ac grids without an intermediate dc link. A matrix converter-type topology is proposed in [7], where 54 switches are needed to realize a three-phase power flow. However, reaching a 95%–98 % efficiency in this SST can be very challenging due to the high switch count [1]. Some other three-phase topologies employing DABs are also proposed in [5], [8], [9], and [11] to reduce the switch count.

There are other conventional SST types [12], [13], [14], [15], [16], which are classified as cascaded-type architectures and often employ an ac–dc–ac or ac–dc–dc–ac stages. In one of

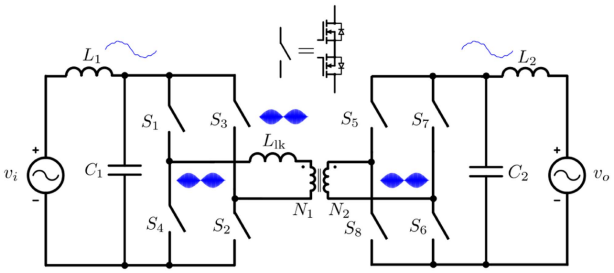

Fig. 1. AC–AC DAB schematic showing frequency components.

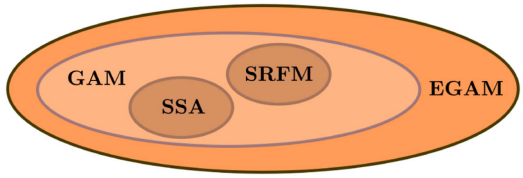

Fig. 2. Various modeling techniques.

these categories, the isolated side sees a high-voltage ac while the dc-link sees a low-voltage dc, which is further inverted. The availability of a dc-link makes these classes of SSTs versatile and facilitates the integration of renewable resources operating at different voltage levels but it also poses challenges due to the higher number of power stages and corresponding circuit complexity [17].

An SST in a dual active bridge (DAB) configuration referred to as the ac–ac DAB in this article is shown in Fig. 1 [6], [17], [18], [19], [20], [21]. This particular topology is an attractive alternative to the cascaded converter architecture [1], [17], [18] because of the following.

1) Fewer passive components.
2) Better reliability.
3) Smaller footprint and lower cost.
4) Soft-switching capability.
5) Higher efficiency.
6) Bidirectional active and reactive power flow capability.
7) Higher safety from galvanic isolation between grids.

Switches S_1–S_4 comprise the primary bridge and S_5–S_8 comprise secondary side bridge. Each switch is a four-quadrant switch [22] with antiseries connected solid-state switches. Two power quality conditioning *LC filters* comprising capacitors L_1 and C_1 on the input side and L_2 and C_2 on the output side are used. The high-frequency transformer provides the isolation and voltage boost/buck actions to interface two different voltage grids. N_1 and N_2 are the HFT primary and secondary turns, respectively. The DAB inductance L_{lk} is a critical parameter for the power transfer between both bridges.

Modeling the dynamic performance of power converters leads to interesting insights into the inner workings of the converters and aids in better understanding. Also, an accurate converter model helps in the design of an appropriate controller for the converter. There are various methods for dynamical system modeling in power electronics: the state space averaging (SSA) technique, the generalized average modeling technique (GAM) [23], [24], [25], the 2-D GAM (2D-GAM) technique [26], [27], [28], and the extended GAM (EGAM) technique [29]. SSA applies when small ripple approximation (SRA) applies to the state variables as is the case with buck, boost, and buck-boost topologies [30]. GAM technique, on the other hand, can model systems whose state variables violate SRA, such as the dc–dc DAB converters [31], [32], [33], [34] and resonant converters [23], [35]. Although improved versions of GAM are proposed [32], [36], it cannot handle two distinct frequencies of excitation. In addition, GAM model proposed for a triple phase shift modulated dc–dc DAB converter [33] handles only single excitation frequency and its subsequent harmonics. In addition, even though GAM representation is used in [20] and [21] to model the ac–ac DAB dynamics, only switching frequency first harmonic approximation is considered, with no explicit inclusion of grid frequency components to model the dynamics. 2D-GAM is applicable where two frequencies of excitations are present, such as the sine pulsewidth modulated inverter with dynamic elements on the ac side [28].

All the aforementioned dynamic modeling techniques approximate the state variables as Fourier series expansions with varying depths of complexity. For example, the SSA technique is a subset of GAM that only tracks the cycle average of state variables and therefore only captures the dc terms in the Fourier series representation. GAM on the other hand also captures the harmonics of the switching functions and ripple behaviors represented as 1-D Fourier series. The popular synchronous reference frame modeling (SRFM) technique used in three-phase inverters [37] is a subset of the GAM and disjoint from the SSA technique. SRFM considers the fundamental components of the state variables involved in the system. Finally, the 2D-GAM technique expands the GAM technique on a second dimension to capture two-frequency behaviors by modeling the state variables as double Fourier series (DFS) representations. Therefore, 2D GAM is a superset modeling technique encompassing GAM and SSA techniques. Therefore, instead of explicitly capturing the time domain behavior of the signals, all these techniques capture the time evolution of Fourier coefficients of the state variables.

Although 2D-GAM effectively captures two-frequency dynamic phenomena, it does not include the multiplication of two DFS variables. Therefore, the authors of past works neglected these DFS product interactions and made the systems simple to circumvent the problem of DFS multiplications. The EGAM technique includes these terms and avoids oversimplification. The EGAM framework uses a discrete Fourier image (DFI) signal to capture the DFS coefficient terms and makes multiplication operations feasible. Fig. 2 shows a venn diagram of various modeling techniques.

In the past, the 2D-GAM and EGAM techniques were used to model the behaviors of single-phase and three-phase inverters [26], [27], [28], [29], [38], [39], [40]. However, the applicability of the EGAM technique for modeling an ac–ac DAB is yet to be explored. The ac–ac DAB also has multifrequency interactions, as shown in Fig. 1, which lead to DFS modeling requirements in the state variables. The inductors L_1 and L_2 and capacitors C_1 and C_2 predominantly experience grid level harmonics while L_{lk} experiences both grid level and

switching level harmonics as shown by the enveloped sinusoidal waveforms in Fig. 1. This article explores the EGAM technique implementation on the ac–ac DAB and compares the results' efficacy with simulation and hardware results. Also, the various insights on the results will be interpreted. The rest of this article is organized as follows. A review of the GAM, 2D-GAM, and EGAM is first presented in Section II. Equipped with the background, the article then models the ac–ac DAB converter in Section III and formulates the EGAM model of the converter. The simulation results are compared with PLECS simulations in Section IV. A hardware converter is designed, and the EGAM results are compared with the hardware results in Section V. Finally, Section VI concludes this article.

II. Review of GAM

In conventional GAM, the time-dependent state variables are transformed to the Fourier coefficients written as single Fourier series (SFS) expansions; that is, a periodic signal $x(t)$ with a fundamental angular frequency ω_0 in the time domain can be written as

$$x(t) = x_0 + \sum_{f\in\mathbb{W}} \{x_{fc}\cos(f\omega_0 t) + x_{fs}\sin(f\omega_0 t)\} \tag{1}$$

where the subscripts c and s correspond to the cos and sin terms of the expansion in rectangular form, respectively. The function vector $\mathbf{C}(t)$ is given by

$$\mathbf{C}(t) = [1 \quad \cos(\omega_0 t) \quad \sin(\omega_0 t) \quad \cdots \quad \cos(f\omega_0 t) \quad \sin(f\omega_0 t)] \tag{2}$$

then (1) can be written in vectorized form as

$$x(t) = \mathbf{C}(t)\cdot\mathbf{x}_f^{\intercal} \tag{3}$$

where $\mathbf{x}_f$ is the vector of Fourier coefficients upto $n\in\mathbb{W}$ indices

$$\mathbf{x}_f = [x_0 \quad x_{1c} \quad x_{1s} \quad \cdots \quad x_{nc} \quad x_{ns}]. \tag{4}$$

With these base relationships, the framework can be extended for other operators [23], [25], [28] given by

$$\frac{d}{dt}\langle x\rangle_f(t) = \left\langle \frac{d}{dt}x \right\rangle_f(t) - jf\omega_0\langle x\rangle_k(t) \tag{5}$$

$$\langle xy\rangle_f = \sum_{i=-\infty}^{\infty}\langle x\rangle_{f-i}\langle y\rangle_i. \tag{6}$$

The operator $\langle\bullet\rangle_f$ represents the fth harmonic Fourier coefficient average value of a time domain signal and (6) is a discrete 1-D convolution [41]. With these base equations, a first-order differential equation of the form

$$\frac{dx(t)}{dt} = ax(t) + by(t) \tag{7}$$

can be rewritten in the Fourier coefficients and using (3)

$$\left\langle \frac{dx(t)}{dt} \right\rangle = a\langle x(t)\rangle + b\langle y(t)\rangle \tag{8}$$

$$\frac{d\mathbf{x}}{dt} = (a\mathbf{I} - \mathbf{T})\mathbf{x} + b\mathbf{y} \tag{9}$$

where $\mathbf{x}$ and $\mathbf{y}$ are SFS Fourier coefficient vectors at the same frequencies. Applying the same procedure on a more complicated base first-order ordinary differential equation

$$\frac{dx(t)}{dt} = ax(t) + bx(t)y(t) \tag{10}$$

translates from time domain to GAM domain to give

$$\frac{d\mathbf{x}}{dt} = (a\mathbf{I} - \mathbf{T})\mathbf{x} + b(\mathbf{x} * \mathbf{y}[\ell]) \tag{11}$$

where $\bullet * \bullet[\bullet]$ represents 1D convolution operator. Equation (11) can then be expanded for the desired number of harmonics Q considered (by writing for each harmonic order, $\ell \in (1, 2, \ldots, Q)$) to finally give

$$\frac{d}{dt}\begin{bmatrix} x_0 \\ x_{1c} \\ x_{1s} \\ \vdots \\ x_{lc} \\ x_{ls} \end{bmatrix} = \begin{bmatrix} a & 0 & 0 & 0 & \cdots & 0 \\ 0 & a & -\omega_1 & 0 & \cdots & 0 \\ 0 & \omega_1 & a & 0 & \cdots & 0 \\ \vdots & \vdots & \vdots & \ddots & \vdots & \vdots \\ 0 & 0 & 0 & 0 & a & -\omega_l \\ 0 & 0 & 0 & 0 & \omega_l & a \end{bmatrix}\begin{bmatrix} x_0 \\ x_{1c} \\ x_{1s} \\ \vdots \\ x_{lc} \\ x_{ls} \end{bmatrix} + b\begin{bmatrix} \sum_{u=-\infty}^{\infty} x[u]y[-u] \\ \Re\{\sum_{u=-\infty}^{\infty} x[u]y[1-u]\} \\ \Im\{\sum_{u=-\infty}^{\infty} x[u]y[1-u]\} \\ \vdots \\ \Re\{\sum_{u=-\infty}^{\infty} x[u]y[l-u]\} \\ \Im\{\sum_{u=-\infty}^{\infty} x[u]y[l-u]\} \end{bmatrix}. \tag{12}$$

In (10), the product of two SFS terms, $x(t)y(t)$, translated to 1-D discrete convolution on the frequency plane for the Fourier coefficient vectors $\mathbf{x}$ and $\mathbf{y}$ [23], [25], [38], [39], [42]. The translation from the time domain to the frequency domain for the multiplication of two terms expressed as DFS is performed using the 2-D convolution of DFI signals [29]. The 2D-GAM [27], along with the addition of the DFI convolution algorithm, forms the EGAM framework.

If the system of interest has two distinct excitation frequencies, namely ω_ζ, ω_χ, the state variable $x(t)$ in the time domain is represented using DFS given by

$$x(t) = \sum_{p\in\mathbb{Z}, r\in\mathbb{W}} \mathrm{x}_{p,r} e^{i(p\omega_\zeta t + r\omega_\chi t)} \tag{13}$$

then it can be converted to the vector containing the Fourier coefficients for a finite number of harmonics as

$$\mathbf{x} = \begin{bmatrix} \mathrm{x}_{0,0} & \mathrm{x}_{1,0c} & \mathrm{x}_{1,0\,s} & \cdots & \mathrm{x}_{0,1c} & \mathrm{x}_{0,1\,s} & \cdots & \mathrm{x}_{p,rc} & \mathrm{x}_{p,rs} \end{bmatrix} \tag{14}$$

where, $\mathrm{x}_{p,0c}$ and $\mathrm{x}_{p,0\,s}$ belong to the Fourier coefficients of the harmonics of ω_ζ; $\mathrm{x}_{0,rc}$ and $\mathrm{x}_{0,rs}$ belong to coefficients of the harmonics of ω_χ, and $\mathrm{x}_{p,rc}$ and $\mathrm{x}_{p,rs}$ belong to coefficients of the harmonics of $p\omega_\zeta + r\omega_\chi$ components.

TABLE I
EGAM OPERATIONS SET

Operation	Time Domain	Frequency Domain
Scalar Product	$ax(t)$	$a\mathbf{x}$
Summation	$x(t)+y(t)$	$\mathbf{x}+\mathbf{y}$
Differentiation	$\frac{dx(t)}{dt}$	$\left(\frac{d\mathbf{x}}{dt}+\mathbf{T}\mathbf{x}\right)$
Multiplication	$x(t)y(t)$	$\mathbf{x}\circledast\circledast\mathbf{y}$

In order to extend the GAM framework to 2D-GAM, the differentiation operator (5) is rewritten as

$$\frac{dx(t)}{dt}=\mathbf{C}(t)\left(\frac{d\mathbf{x}}{dt}+\mathbf{T}\mathbf{x}\right) \tag{15}$$

where $\mathbf{C}(t)$ is rewritten for two frequencies and the DFS coefficients of the expansion are stored in the state variable $\mathbf{x}$ (14). The matrix $\mathbf{T}$ stores the frequency information at the state variable $\mathrm{x}_{p,r}$. Therefore, $\mathbf{T}$ is the matrix version of the second term of the differentiation operator in SFS (5) given by

$$\mathbf{T}_{(2\,k,2k+1)}=(\mathbf{m}_{k+1}\omega_\zeta+\mathbf{n}_{k+1}\omega_\chi) \tag{16}$$

$$\mathbf{T}_{(2k+1,2\,k)}=-(\mathbf{m}_{k+1}\omega_\zeta+\mathbf{n}_{k+1}\omega_\chi) \tag{17}$$

where $k\in\mathbb{N}^O$, indexes the vectors $\mathbf{m}\in\mathbb{Z}^{O+1}$, and $\mathbf{n}\in\mathbb{W}^{O+1}$. Dimensionally, $\mathbf{T}$ is a $(2O+1)\times(2O+1)$ sparse matrix [27]. O is the total number of distinct frequencies and harmonic combinations considered, excluding the dc term and $k\in\{1,2,\cdots O\}$. Vectors $\mathbf{m}$ and $\mathbf{n}$ have an order of one more than the distinct frequencies (O) to account for the dc term, which is always the first entry from an indexing viewpoint. Referring back to (10), and assuming $x(t)$ and $y(t)$ to be DFS expansions instead of SFS, (11) can be expanded into the second dimension by

$$\frac{d\mathbf{x}}{dt}=(a\mathbf{I}-\mathbf{T})\mathbf{x}+b(\mathbf{x}\circledast\circledast\mathbf{y}) \tag{18}$$

where $\bullet\circledast\circledast\bullet$ operator signifies the 2D DFI convolution algorithm [29] operation. This completes the EGAM formulation that is capable of handling DFS products. A complete set of the time domain to EGAM translations is given in Table I for clarity.

III. DYNAMIC MODEL OF AC–AC DAB

A. Switching Function Fourier Series Representation

Before proceeding with the dynamic equations of the ac–ac DAB converter, the switching function $q_+(t)$ for the phase shift modulated pulsewidth modulation (PWM) must be realized. The switching function for a switching angular frequency of $\omega_s=2\pi f_s$ and phase shift angle $\phi\,\mathrm{rad}$ is given by

$$q_+(t)=\begin{cases}1, & -\pi<\omega_s t<-\pi+\phi\\ 0, & -\pi+\phi<\omega_s t<\phi\\ 1, & \phi<\omega_s t<\pi.\end{cases} \tag{19}$$

The periodic signal $q_+(t)$ can be expanded as a Fourier series representation as

$$q_+(t)=a_0+\sum_{n=1}^{\infty}a_n\cos(nt)+\sum_{n=1}^{\infty}b_n\sin(nt) \tag{20}$$

where a_0, a_n, and b_n are the Fourier coefficients given by

$$\begin{aligned}a_0&=\frac{1}{2}\\ a_n(\phi)&=-\frac{\sin(n\pi-n\phi)}{n\pi}-\frac{\sin(n\phi)}{n\pi}\\ b_n(\phi)&=-\frac{\cos(n\pi-n\phi)}{n\pi}+\frac{\cos(n\phi)}{n\pi}.\end{aligned} \tag{21}$$

B. Time Domain Dynamic Equations

The schematic of the ac–ac DAB is shown in Fig. 3. The input voltage $v_i(t)$ and output voltage $v_o(t)$ are grid voltages with a peak value of V_i and V_o, respectively. The input and output voltages have phase angles θ and δ, respectively. An *LC filter* comprising the inductor L_1 and capacitor C_1 is used on the primary side. The secondary side is comprised of another *LC filter* with the inductor L_2 and capacitor C_2. Both the inductors have internal resistances R_{L_1} and R_{L_2}. A transformer links the primary side H-bridge with the secondary side H-bridge. The transformer has a leakage inductance L_{lk} and a winding resistance R_t. The transformer has a turns ratio given by $N=N_1/N_2$ where N_1 and N_2 are the transformer's primary and secondary turns count, respectively.

Five dynamic equations can be written as there are five dynamical elements in the system. By writing the node and mesh equations for the circuit, the dynamic equations turn out to be

$$\frac{di_{L_1}(t)}{dt}=\frac{1}{L_1}v_i(t)-\frac{R_L}{L_1}i_{L_1}(t)-\frac{1}{L_1}v_{C_1}(t) \tag{22}$$

$$\frac{dv_{C_1}(t)}{dt}=\frac{1}{C_1}i_{L_1}(t)-\frac{1}{C_1}i_{L_{lk}}(t)\Delta q_1(t) \tag{23}$$

$$\frac{di_{L_{lk}}(t)}{dt}=\frac{v_{C_1}(t)}{L_{lk}}\Delta q_1(t)-\frac{Nv_{C_2}(t)}{L_{lk}}\Delta q_2(t)-\frac{R_t}{L_{lk}}i_{lk}(t) \tag{24}$$

$$\frac{di_{L_2}(t)}{dt}=\frac{1}{L_2}v_o(t)-\frac{R_{L_2}}{L_2}i_{L_2}(t)-\frac{1}{L_2}v_{C_2}(t) \tag{25}$$

$$\frac{dv_{C_2}(t)}{dt}=\frac{i_{L_2}(t)}{C_2}+\frac{Ni_{lk}(t)}{C_2}\Delta q_2(t) \tag{26}$$

where $\Delta q_1(t)$ and $\Delta q_2(t)$ are the primary and secondary side H-Bridge actions, respectively. The function $\Delta q_d(t)$ is expanded as $q_{d+}(t)-q_{d-}(t)$ for $d\in\{1,2\}$. The complement of $q_{d+}(t)$ is denoted by $q_{d-}(t)$. The H-bridge is modeled as a transformer with a turns ratio of $\Delta q_d(t)$, and the currents and voltages across the H-bridge are related by energy equivalence.

C. EGAM Dynamic Equations

For transforming the time domain differential equations to the frequency domain, the EGAM operators in Table I are used. The switching term $\Delta q_d(t)$ transform to $\mathbf{q}_{d+}-\mathbf{q}_{d-}$, which can be further simplified to $2\mathbf{q}_{d+}-\Upsilon$, where Υ is a sparse vector given by

$$\Upsilon=\begin{bmatrix}1 & 0 & 0 & \cdots & 0\end{bmatrix}. \tag{27}$$

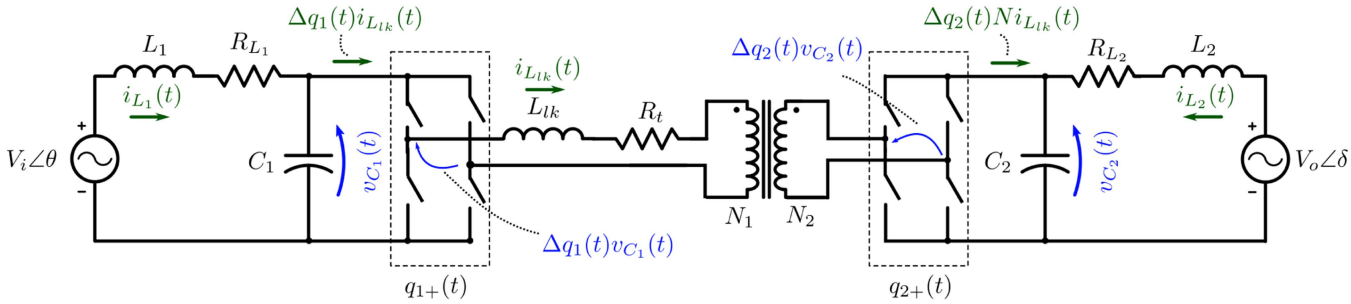

Fig. 3. AC–AC DAB schematic for EGAM formulation.

For $\mathbf{q}_{1+}$, the relationships in (21) with $\phi = 0$ is used, as $\mathbf{q}_{1+}$ is the primary side switching function serving as the zero reference. For secondary side, $\mathbf{q}_{2+}$ is written for $\phi \in \{-\pi/2, +\pi/2\}$. The $\mathbf{q}_{d+}$ switching vectors are given by

$$\mathbf{q}_{d+} = \begin{bmatrix} a_0 & a_1(\phi) & b_1(\phi) & \cdots & a_n(\phi) & b_n(\phi) \end{bmatrix}. \tag{28}$$

Using these transformations, the frequency domain dynamic equations are given by

$$\frac{d\mathbf{i}_{L_1}}{dt} = -\left(\frac{R_{L_1}}{L_1} + \mathbf{T}\right)\mathbf{i}_{L_1} + \frac{1}{L_1}\Gamma - \frac{1}{L_1}\mathbf{v}_{C_1} \tag{29}$$

$$\frac{d\mathbf{v}_{C_1}}{dt} = -\mathbf{T}\mathbf{v}_{C_1} + \frac{1}{C_1}\mathbf{i}_{L_1} - \frac{1}{C_1}(2\mathbf{i}_{L_{lk}} \circledast \circledast \mathbf{q}_{1+} - \mathbf{i}_{L_{lk}} \circledast \circledast \Upsilon) \tag{30}$$

$$\frac{d\mathbf{i}_{L_{lk}}}{dt} = -\left(\frac{R_t}{L_{lk}} + \mathbf{T}\right)\mathbf{i}_{lk} + \frac{1}{L_{lk}}(2\mathbf{v}_{C_1} \circledast \circledast \mathbf{q}_{1+} - \mathbf{v}_{C_1} \circledast \circledast \Upsilon) - \frac{N_1}{N_2}\frac{1}{L_{lk}}(2\mathbf{v}_{C_2} \circledast \circledast \mathbf{q}_{2+} - \mathbf{v}_{C_2} \circledast \circledast \Upsilon) \tag{31}$$

$$\frac{d\mathbf{i}_{L_2}}{dt} = -\left(\mathbf{T} + \frac{R_{L_2}}{L_2}\right)\mathbf{i}_{L_2} + \frac{1}{L_2}\Lambda - \frac{1}{L_2}\mathbf{v}_{C_2} \tag{32}$$

$$\frac{d\mathbf{v}_{C_2}}{dt} = -\mathbf{T}\mathbf{v}_{C_2} + \frac{\mathbf{i}_{L_2}}{C_2} + \frac{1}{C_2}(2\mathbf{i}_{lk} \circledast \circledast \mathbf{q}_{2+} - \mathbf{i}_{lk} \circledast \circledast \Upsilon) \tag{33}$$

where Γ and Λ are referred to as excitation vectors, which carry the information of the grid voltage excitation. These vectors are sparse, with values populated only at frequency indices where excitations are present. The excitation vectors for an input peak voltage V_i and input phase angle θ and output peak voltage V_o with phase angle δ are given by

$$\begin{aligned} \Gamma &= \begin{bmatrix} 0 & \cdots & V_i\sin(\theta) & V_i\cos(\theta) & \cdots & 0 \end{bmatrix} \\ \Lambda &= \begin{bmatrix} 0 & \cdots & V_o\sin(\delta) & V_o\cos(\delta) & \cdots & 0 \end{bmatrix}. \end{aligned} \tag{34}$$

D. DFS Product Term Expansion

The product terms $\mathbf{a} \circledast \circledast \mathbf{b}$ can be expanded for analysis, where $\mathbf{a}$, $\mathbf{b}$ are two DFS coefficient vectors. Various expansions can be written based on the number of p-axis and r-axis harmonics. One such expansion is given here. For a p-axis range of one grid fundamental and r-axis range of one switching harmonic, the DFS vectors are given by

$$\mathbf{a} = \begin{bmatrix} a_{00} & a_{01c} & a_{01\,s} & a_{10c} & a_{10\,s} & a_{11c} & a_{11\,s} & a_{-11c} & a_{-11\,s} \end{bmatrix} \tag{35}$$

$$\mathbf{b} = \begin{bmatrix} b_{00} & b_{01c} & b_{01\,s} & b_{10c} & b_{10\,s} & b_{11c} & b_{11\,s} & b_{-11c} & b_{-11\,s} \end{bmatrix}. \tag{36}$$

Let the convolution result of $\mathbf{a} \circledast \circledast \mathbf{b}$ be α given by

$$\alpha = \begin{bmatrix} \alpha_{00} & \alpha_{01c} & \alpha_{01\,s} & \alpha_{10c} & \alpha_{10\,s} & \alpha_{11c} & \alpha_{11\,s} & \alpha_{-11c} & \alpha_{-11\,s} \end{bmatrix} \tag{37}$$

where

$$\begin{aligned} \alpha_{00} &= a_{00}b_{00} + \frac{1}{2}\Big[a_{01c}b_{01c} + a_{10c}b_{10c} + a_{11c}b_{11c} + a_{01\,s}b_{01\,s} \\ &\quad + a_{10\,s}b_{10\,s} + a_{11\,s}b_{11\,s} + a_{-11\,s}b_{-11\,s} + a_{-11c}b_{-11c}\Big] \\ \alpha_{01c} &= a_{00}b_{01c} + a_{01c}b_{00} + \frac{1}{2}\Big[a_{10c}b_{11c} + a_{11c}b_{10c} + a_{10\,s}b_{11\,s} \\ &\quad + a_{11\,s}b_{10\,s} + a_{10c}b_{-11c} + a_{-11c}b_{10c} \\ &\quad + a_{10\,s}b_{-11\,s} + a_{-11\,s}b_{10\,s}\Big] \\ \alpha_{01\,s} &= a_{00}b_{01\,s} + a_{01\,s}b_{00} + \frac{1}{2}\Big[a_{10c}b_{11\,s} \\ &\quad - a_{11c}b_{10\,s} - a_{10\,s}b_{11c} + a_{11\,s}b_{10c} + a_{10c}b_{-11\,s} \\ &\quad + a_{10\,s}b_{-11c} + a_{-11c}b_{10\,s} + a_{-11\,s}b_{10c}\Big] \\ \alpha_{10c} &= a_{00}b_{10c} + a_{10c}b_{00} + \frac{1}{2}\Big[a_{01c}b_{11c} + a_{11c}b_{01c} \\ &\quad + a_{01\,s}b_{11\,s} + a_{11\,s}b_{01\,s} + a_{01c}b_{-11c} \\ &\quad + a_{-11c}b_{01c} + a_{01\,s}b_{-11\,s} + a_{-11\,s}b_{01\,s}\Big] \\ \alpha_{10\,s} &= a_{00}b_{10\,s} + a_{10\,s}b_{00} + \frac{1}{2}\Big[a_{01c}b_{11\,s} - a_{11c}b_{01\,s} \\ &\quad - a_{01\,s}b_{11c} + a_{11\,s}b_{01c} - a_{01c}b_{-11\,s} \\ &\quad + a_{01\,s}b_{-11c} + a_{-11c}b_{01\,s} - a_{-11\,s}b_{01c}\Big] \end{aligned}$$

TABLE II
AC–AC DAB EXPERIMENTAL PARAMETERS

Parameter	Value
f_{sw}	30 kHz
f_g	60 Hz
$L_1 = L_2$	270 μH
$R_{L_1} = R_{L_2}$	100 mΩ
$C_1 = C_2$	40 μF
L_{lk}	10 μF
R_t	10 mΩ
$N_1 = N_2$	1

TABLE III
EGAM PERFORMANCE IMPROVEMENT TO INCREASE IN SWITCHING HARMONICS

Case	MAE (PLECS versus EGAM)	% improvement over first case
$p = 1, r = 1$	1.1	0
$p = 1, r = 3$	0.681	38.12
$p = 1, r = 5$	0.411	62.68

$$\alpha_{11c} = a_{00}b_{11c} + a_{11c}b_{00} + \frac{1}{2}\Big[a_{01c}b_{10c} + a_{10c}b_{01c} - a_{01\,s}b_{10\,s} - a_{10\,s}b_{01\,s}\Big]$$

$$\alpha_{11\,s} = a_{00}b_{11\,s} + a_{11\,s}b_{00} + \frac{1}{2}\Big[a_{01c}b_{10\,s} + a_{10c}b_{01\,s} + a_{01\,s}b_{10c} + a_{10\,s}b_{01c}\Big]$$

$$\alpha_{-11c} = a_{00}b_{-11c} + a_{-11c}b_{00} + \frac{1}{2}\Big[a_{01c}b_{10c} + a_{10c}b_{01c} + a_{01\,s}b_{10\,s} + a_{10\,s}b_{01\,s}\Big]$$

$$\alpha_{-11\,s} = a_{00}b_{-11\,s} + a_{-11\,s}b_{00} + \frac{1}{2}\Big[a_{10c}b_{01\,s} - a_{01c}b_{10\,s} + a_{01\,s}b_{10c} - a_{10\,s}b_{01c}\Big].$$

IV. SIMULATION VERIFICATION

In this section, a PLECS model is created to act as a baseline to compare the performance of various EGAM models of the ac–ac DAB. The EGAM model developed in the earlier section is used, and simulations are run for the same conditions in the PLECS and EGAM simulations. The parameters used in simulation studies are given in Table II .

The DFI convolution algorithm is developed using the EGAM toolbox [43] and is used to simulate the ac–ac DAB converter. A startup sequence is first simulated for a ϕ value of 25 ° applied between the H-bridges for a preexcited system with an RMS voltage of 30 V for v_i and v_o.

Initially, the simulation results for $p = 1$ and $r = 1$ are performed. Fig. 4(a) shows v_{C_1} voltages for the startup sequence for the aforementioned harmonic components. The current $i_{L_1}(t)$ is shown in Fig. 4(b). Although the capacitor voltage shows a good match between PLECS and EGAM simulations, slight mismatches can be seen in the zoomed versions of the same plots shown below the main plots. The inductor currents also show appreciable congruence between PLECS and EGAM simulations. As power flows from the primary to the secondary side due to a positive phase shift, the currents in inductors are antiphase. However, the steady-state amplitude of the inductor currents for EGAM results is slightly less than their PLECS counterparts. This mismatch in current is associated with the harmonics considered in the EGAM simulation. As the fundamental switching harmonic is the only component considered for simulation, the power transfer at the fundamental harmonic is only shown in the filter inductors at the grid level. Therefore, higher order harmonics must be considered to improve model matching.

In order to achieve higher matching accuracy in the EGAM and PLECS results, simulations are performed for $p = 1$ and $r = 3$ model so that the third harmonic switching actions are also considered. Therefore, the harmonic truncation [29] boundary expands until the third harmonic, leading to better features in the state variables. The results in Fig. 4(c) shows better matching characteristics after startup in the capacitor state. Fig. 4(d) shows better model accuracy in transient and steady-state behaviors for the inductor state. The third harmonic power transfer at the switching frequency improves current matching in the filter inductor currents.

The leakage inductor current waveform for PLECS and EGAM simulations is shown in Fig. 5. The waveforms show an excellent match with the PLECS simulation and thereby prove the efficacy of the EGAM framework for modeling multifrequency excitations. In addition, Fig. 6 shows the performance of EGAM for various harmonic truncation boundaries enforced inside the EGAM model. As the number of switching (r axis) harmonics increases, the EGAM performance approaches closer to the PLECS benchmark waveform.

To quantify the improvements of EGAM models with various levels of harmonic depths, mean absolute error (MAE) is computed between PLECS-simulated (baseline) and the EGAM-simulated outputs. MAE is given by

$$\text{MAE} = \frac{\sum_{i=1}^{L} \mid u_i - v_i \mid}{L} \tag{38}$$

where u is the predicted value, v is the baseline value, and L is the length of the window for comparison. The comparisons are made between the PLECS simulated values v and each EGAM simulation values u. The MAE results for each simulation are shown in Table III.

Another example is provided to show how dropping the 2-D convolution operator causes significant errors in modeling. The i_{L1} inductor current's startup simulation is shown in Fig. 7. The EGAM simulation with $r = 3$ included has a significantly different behavior than the model with $r = 0$. Dropping the switching frequency term (i.e., making $r = 0$) makes the EGAM model transform to a GAM model. As the DAB transfers power primarily in the grid-switching frequency side bands, ignoring them leads to the conventional GAM, which cannot capture multifrequency interactions. On the other hand, EGAM captures the phenomenon very well.

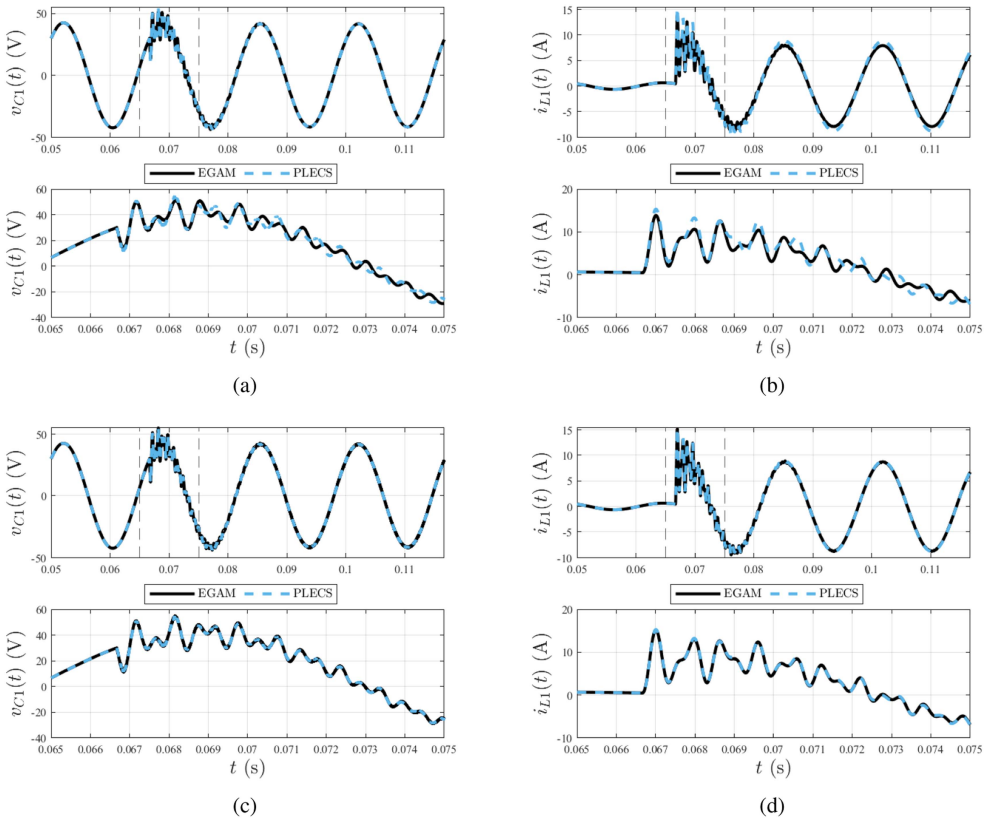

Fig. 4. Comparison between HAD GAM and detailed simulation model for a single phase inverter dynamics. (a) C_1 voltage for startup sequence, $p = 1$ and $r = 1$. (b) L_1 current for startup sequence, $p = 1$ and $r = 1$. (c) C_1 voltage for startup sequence, $p = 1$ and $r = 3$. (d) L_1 current for startup sequence, $p = 1$ and $r = 3$.

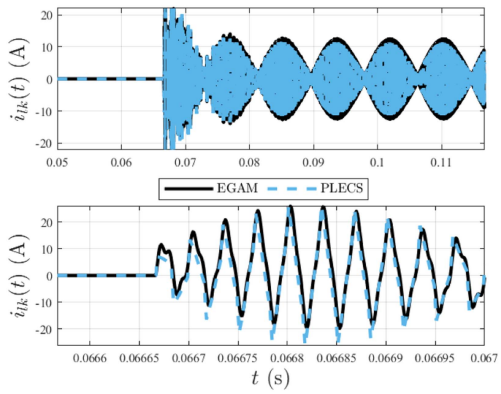

Fig. 5. Leakage inductor current startup performance for $p = 1$ and $r = 3$ EGAM simulation overlayed on PLECS simulation.

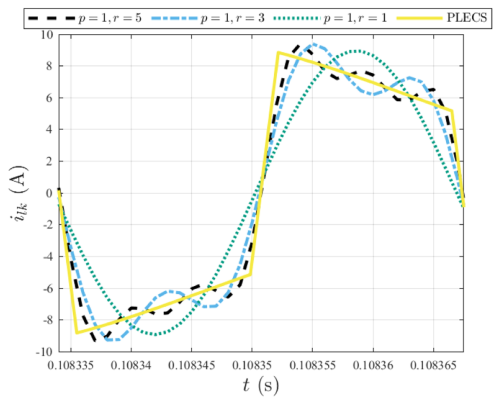

Fig. 6. Leakage inductor current steady state performance for EGAM simulation overlayed on PLECS simulation for various orders of harmonic truncation.

A. *Frequency Plane Plots*

The vectors in the frequency domain time progression matrix $\mathbf{x}$ for $\mathbf{x} \in \{\mathbf{i}_{L_1}, \mathbf{i}_{L_{lk}}\}$ are transformed into the time domain using the frequency to time domain transformation (3). To understand the harmonic nature of the state variables, each component of $\mathbf{x}$ is plotted over time. As the harmonic components other than the dc term have both the sine and the cosine coefficients, their magnitude is computed to get the behavior of the state variable at each frequency of interest.

The ac–ac DAB's state variables are plotted against time to understand the harmonic behaviors of the state variables. The results for inductor L_1 current in frequency plane $\mathbf{i}_{L_1}$ are shown in Fig. 8. The simulation for one grid harmonic and three switching harmonics is performed. The first number subscript on the y-axis label on each plot indicates the grid frequency harmonic while the second index indicates the switching frequency harmonics. The EGAM plots indicate no activity in the dc and pure switching frequency harmonics. This is associated with the absence of excitation voltages in the switching frequency indices in the

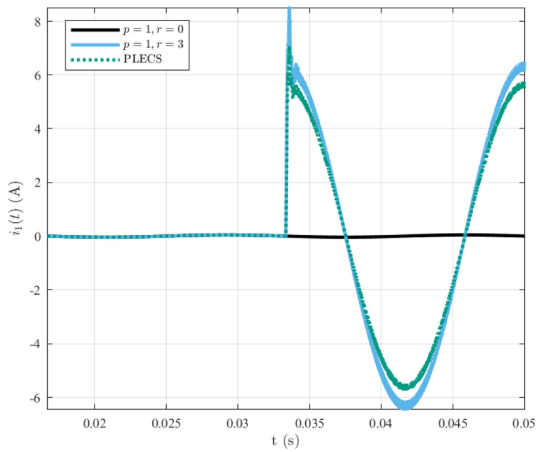

Fig. 7. Effect of ignoring the ⊛ ⊛ term in $i_{L1}(t)$ current.

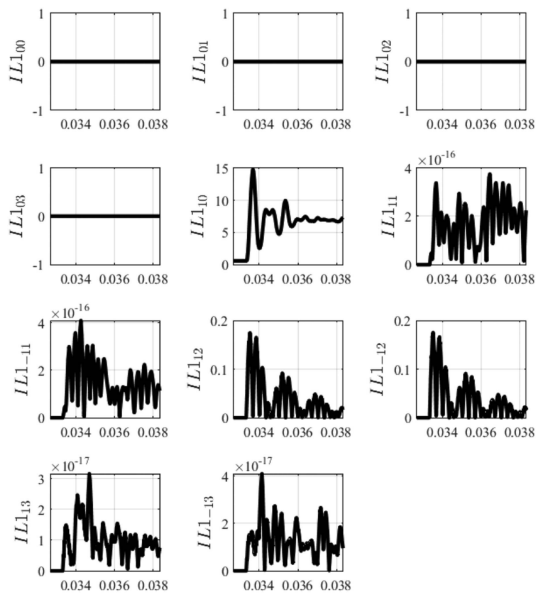

Fig. 8. Harmonic components of $\mathbf{i}_{L_1}$.

excitation vectors (34). The grid frequency component ($IL1_{10}$) is the most significant harmonic in the plots. In addition, Fig. 9 plots the current characteristics at different harmonic indices for $\mathbf{i}_{L_{1k}}$. Like the grid side inductor, the leakage inductor harmonic waveforms show no activity at the dc component. However, it is interesting to note that there are no switching frequency components present in $i_{lk}(t)$. This is associated with the convolution operations and the emergence of new frequency components. This explains the significant activity in the Ilk_{11}, Ilk_{-11}, Ilk_{13}, and Ilk_{-13} components where the new behaviors are seen. The $i_{lk}(t)$ waveform is an amplitude-modulated waveform where the switching frequency component is enveloped by the grid frequency, leading to the $f_g \pm nf_s$; $n \in \mathbb{N}$ components having the dominant behavior.

V. Hardware Implementation

In this section, a hardware model is built and tests similar to those done in Section IV will be repeated to understand the correctness of the models. For this purpose, an ac–ac DAB

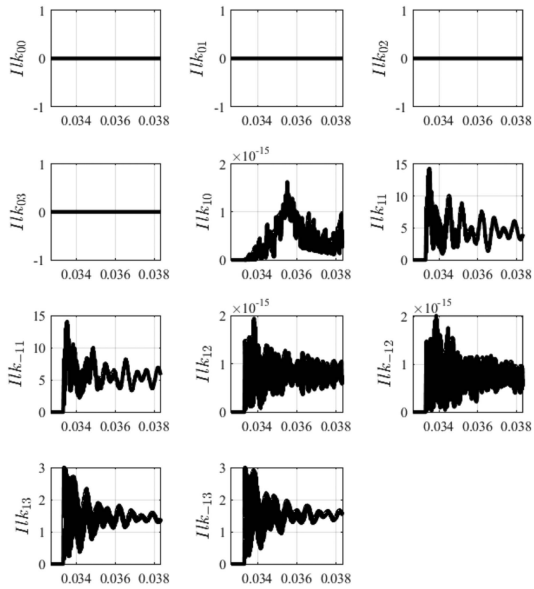

Fig. 9. Harmonic components in $\mathbf{i}_{lk}$.

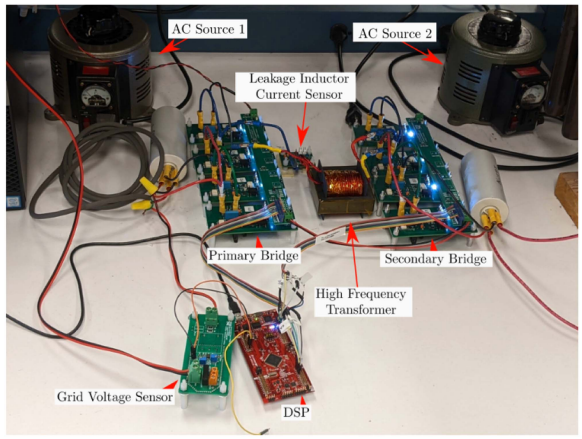

Fig. 10. AC–AC DAB Hardware Setup.

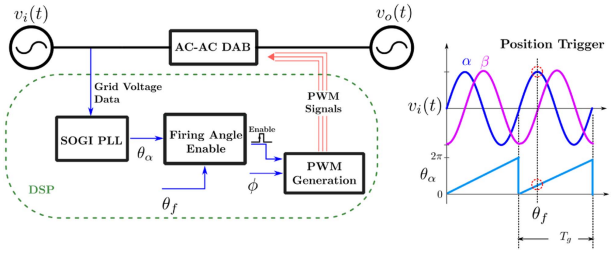

Fig. 11. AC–AC DAB hardware implementation in DSP.

prototype is designed, as shown in Fig. 10, with the specifications in Table. II. To synchronize the trigger of the hardware model at the same time as that of the EGAM and PLECS models, a second-order generalized inverter (SOGI) phase-locked loop (PLL) [44]-based positional trigger is implemented in a TMS320F28377S digital signal processor (DSP), as shown in Fig. 11. The SOGI PLL synchronizes with the grid frequency to get the phase information θ_α. If the position trigger's firing angle θ_f is desired, the θ_α and its match with θ_f is used to set the enable signal. The enable signal is then directed to the DSP's

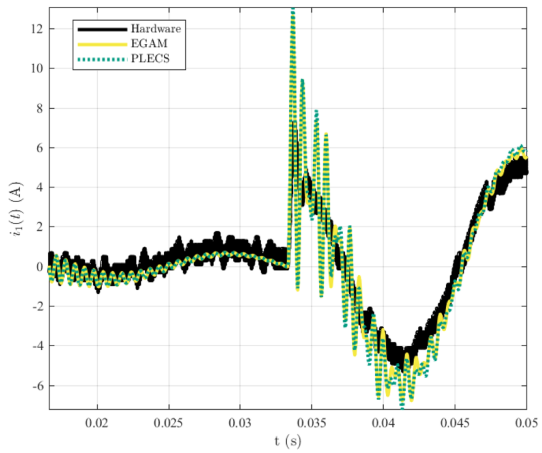

Fig. 12. Inductor L_1 current.

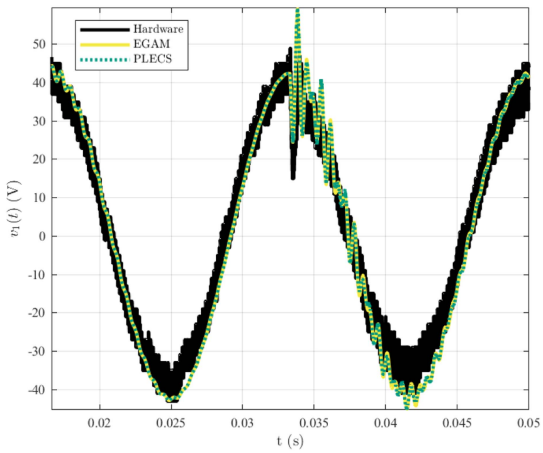

Fig. 13. Capacitor C_1 voltage.

PWM module. The PWM module is configured to perform the phase shift modulation for the DAB stage switches for a preset value of ϕ.

A test is performed with input voltages of $26\,\mathrm{V_{RMS}}$ on both sides of the DAB are used. Two variable auto transformers serve as the ac sources; ac-source-1 and ac source-2. A ϕ of 21.5° is enforced on the DAB. The voltages are converted to peak values and enforced on the excitation vectors (34) with $\theta = \delta = 90^\circ$. The PLECS and EGAM models are run subsequently. The hardware model on the other hand is started at a θ_f of 90°. The acquired results are plotted in Figs. 12 and 13.

VI. Conclusion

This article uses the EGAM modeling framework to model the dynamics of the ac–ac DAB converter. After a brief review of the existing GAM modeling techniques and the EGAM technique, this article uses the EGAM technique to form the dynamic model of the ac–ac DAB. After this, the simulation tests are performed, and the PLECS and EGAM models are overlayed on top of each other. Higher matches with the PLECS waveforms are observed by adding more switching frequency harmonics in the EGAM model, leading to progressively lower MAE values, signifying excellent accuracies. The frequency plane magnitude versus time graph shows the harmonics present at all excitation frequencies and new frequencies in the region of interest. The leakage inductor current is an amplitude-modulated waveform enveloped by the grid frequencies, showing negligible grid frequency and dominant sideband components. It is also shown that at the bridge level, the power transfer takes place at sideband frequencies of the grid and switching frequencies. Finally, the hardware model of the ac–ac DAB converter is constructed, and the state variables are plotted against the EGAM simulations. The model matching is observed, thereby validating the correctness of the EGAM framework and its ability to capture two frequency dynamics. Also, EGAM in the future can be used for the following purposes.

1) As a simulation tool for understanding and identifying the important frequencies of interest at play in a complex system.
2) Understanding the tradeoffs of including or excluding various frequencies to obtain abstractions of power converter dynamics that enable reduced order modeling, control system modeling, and steady-state analysis.
3) A mechanized way of extracting large-signal, small-signal, and transfer function models with various levels of complexity.

Acknowledgment

The authors would like to thank the DOE Office of Electricity Energy Storage Program and Dr. Imre Gyuk for the generous financial support.

References

[1] X. She, A. Q. Huang, and R. Burgos, "Review of solid-state transformer technologies and their application in power distribution systems," *IEEE Trans. Emerg. Sel. Topics Power Electron.*, vol. 1, no. 3, pp. 186–198, Sep. 2013.

[2] F. Bignucolo, M. Bertoluzzo, and C. Fontana, "Applications of the solid state transformer concept in the electrical power system," in *Proc. AEIT Int. Annu. Conf.*, 2015, pp. 1–6.

[3] Q. Zhu, L. Wang, D. Chen, L. Zhang, and A. Q. Huang, "Design and implementation of a 7.2 kV single stage AC-AC solid state transformer based on current source series resonant converter and 15 kV SiC MOSFET," in *Proc. IEEE Energy Convers. Congr. Expo.*, 2017, pp. 1288–1295.

[4] F. Ruiz, M. A. Perez, J. R. Espinosa, T. Gajowik, S. Stynski, and M. Malinowski, "Surveying solid-state transformer structures and controls: Providing highly efficient and controllable power flow in distribution grids," *IEEE Ind. Electron. Mag.*, vol. 14, no. 1, pp. 56–70, Mar. 2020.

[5] H. Chen and D. Divan, "Soft-switching solid-state transformer (S4T)," *IEEE Trans. Power Electron.*, vol. 33, no. 4, pp. 2933–2947, Apr. 2018.

[6] R. Rahmoun and M. Patt, "High efficiency single-phase dual-active-bridge AC/AC converter," in *Proc. 21st Eur. Conf. Power Electron. Appl.*, 2019, pp. P.1–P.10.

[7] K. Mohapatra and N. Mohan, "Matrix converter fed open-ended power electronic transformer for power system application," in *Proc. IEEE Power Energy Soc. Gen. Meeting - Convers. Del. Elect. Energy 21st Century*, 2008, pp. 1–6.

[8] H. Keyhani, H. A. Toliyat, M. Harfman-Todorovic, R. Lai, and R. Datta, "An isolated resonant AC-link three-phase AC–AC converter using a single HF transformer," *IEEE Trans. Ind. Electron.*, vol. 61, no. 10, pp. 5174–5183, Oct. 2014.

[9] K. Basu, A. Shahani, A. K. Sahoo, and N. Mohan, "A single-stage solid-state transformer for PWM AC drive with source-based commutation of leakage energy," *IEEE Trans. Power Electron.*, vol. 30, no. 3, pp. 1734–1746, Mar. 2015.

[10] A. Sharma, K. J. P. Veeramraju, and J. W. Kimball, "Power flow control of a single-stage AC-AC solid-state transformer for AC distribution system," in *Proc. IEEE Power Energy Conf. Illinois*, 2022, pp. 1–6.

[11] A. Prasai et al., "Dyna-C: Experimental results for a 50 kVA 3-phase to 3-phase solid state transformer," in *Proc. IEEE Appl. Power Electron. Conf. Expo.*, 2014, pp. 2271–2277.
[12] J. Ai-juan, L. Hang-tian, and L. Shao-long, "A new matrix type three-phase four-wire power electronic transformer," in *Proc. 37th IEEE Power Electron. Specialists Conf.*, 2006, pp. 1–6.
[13] M. Sabahi, A. Y. Goharrizi, S. H. Hosseini, M. B. B. Sharifian, and G. B. Gharehpetian, "Flexible power electronic transformer," *IEEE Trans. Power Electron.*, vol. 25, no. 8, pp. 2159–2169, Aug. 2010.
[14] E. Ronan, S. Sudhoff, S. Glover, and D. Galloway, "A power electronic-based distribution transformer," *IEEE Trans. Power Del.*, vol. 17, no. 2, pp. 537–543, Apr. 2002.
[15] S. Bhattacharya et al., "Design and development of generation-I silicon based solid state transformer," in *Proc. 25th Annu. IEEE Appl. Power Electron. Conf. Expo.*, 2010, pp. 1666–1673.
[16] D. Gonzalez-Agudelo, A. Escobar-Mejía, and H. Ramirez-Murrillo, "Dynamic model of a dual active bridge suitable for solid state transformers," in *Proc. 13th Int. Conf. Power Electron.*, 2016, pp. 350–355.
[17] H. Qin and J. W. Kimball, "Solid-state transformer architecture using AC–AC dual-active-bridge converter," *IEEE Trans. Ind. Electron.*, vol. 60, no. 9, pp. 3720–3730, Sep. 2013.
[18] H. Qin and J. W. Kimball, "Ac-ac dual active bridge converter for solid state transformer," in *Proc. IEEE Energy Convers. Congr. Expo.*, 2009, pp. 3039–3044.
[19] G. G. Facchinello, L. L. Brighenti, S. L. Brockveld, D. C. Martins, and W. M. D. Santos, "Closed-loop operation and control strategy for the dual active half bridge AC-AC converter," in *Proc. IEEE 8th Int. Symp. Power Electron. Distrib. Gener. Syst.*, 2017, pp. 1–7.
[20] M. A. Tawfik, M. Ehab, A. Ahmed, and J.-H. Park, "Single-stage isolated ac/ac converter with phase-shifted controller," *IEEE Trans. Emerg. Sel. Topics Power Electron.*, vol. 11, no. 2, pp. 1815–1826, Apr. 2023.
[21] M. A. Tawfik, M. Ehab, A. Ahmed, and J.-H. Park, "Single-stage isolated DC/AC converter with continuous dynamic model and controller design," *IEEE Trans. Ind. Electron.*, vol. 70, no. 6, pp. 5971–5981, Jun. 2023.
[22] G. Venkataramanan and N. Kogalur, "A hybrid 4-quadrant switch for AC power conversion," in *Proc. IEEE Energy Convers. Congr. Expo.*, 2019, pp. 5487–5493.
[23] S. Sanders, J. Noworolski, X. Liu, and G. Verghese, "Generalized averaging method for power conversion circuits," *IEEE Trans. Power Electron.*, vol. 6, no. 2, pp. 251–259, Apr. 1991.
[24] L. Wang et al., "Electromagnetic transient modeling and simulation of power converters based on a piecewise generalized state space averaging method," *IEEE Access*, vol. 7, pp. 12241–12251, 2019.
[25] V. Caliskan, O. Verghese, and A. Stankovic, "Multifrequency averaging of DC/DC converters," *IEEE Trans. Power Electron.*, vol. 14, no. 1, pp. 124–133, Jan. 1999.
[26] X. Liu, "Improvements in inverter modeling and control," Ph.D. dissertation, Univ. Kentucky, Lexington, KY, USA, 2017.
[27] X. Liu, A. M. Cramer, and F. Pan, "Generalized average method for time-invariant modeling of inverters," *IEEE Trans. Circuits Syst. I: Regular Papers*, vol. 64, no. 3, pp. 740–751, Mar. 2017.
[28] X. Liu and A. M. Cramer, "Three-phase inverter modeling using multifrequency averaging with third harmonic injection," in *Proc. IEEE Energy Convers. Congr. Expo.*, 2016, pp. 1–6.
[29] K. J. P. Veeramraju, J. A. Mueller, and J. W. Kimball, "An extended generalized average modeling framework for power converters," *IEEE Trans. Power Electron.*, vol. 38, no. 8, pp. 9581–9592, Aug. 2023.
[30] P. Azer and A. Emadi, "Generalized state space average model for multi-phase interleaved buck, boost and buck-boost DC-DC converters: Transient, steady-state and switching dynamics," *IEEE Access*, vol. 8, pp. 77735–77745, 2020.
[31] H. Qin and J. W. Kimball, "Generalized average modeling of dual active bridge DC–DC converter," *IEEE Trans. Power Electron.*, vol. 27, no. 4, pp. 2078–2084, Apr. 2012.
[32] J. A. Mueller and J. W. Kimball, "An improved generalized average model of DC–DC dual active bridge converters," *IEEE Trans. Power Electron.*, vol. 33, no. 11, pp. 9975–9988, Nov. 2018.
[33] M. Rolak, M. Twardy, and C. Soból, "Generalized average modeling of a dual active bridge DC-DC converter with triple-phase-shift modulation," *Energies*, vol. 15, no. 16, 2022, Art. no. 6092. [Online]. Available: https://www.mdpi.com/1996-1073/15/16/6092
[34] S. Shao et al., "Modeling and advanced control of dual-active-bridge DC–DC converters: A review," *IEEE Trans. Power Electron.*, vol. 37, no. 2, pp. 1524–1547, Feb. 2022.
[35] Z. U. Zahid et al., "Modeling and control of series–series compensated inductive power transfer system," *IEEE Trans. Emerg. Sel. Topics Power Electron.*, vol. 3, no. 1, pp. 111–123, Mar. 2015.
[36] B. Liu, P. Davari, and F. Blaabjerg, "An enhanced generalized average modeling of dual active bridge converters," in *Proc. IEEE Appl. Power Electron. Conf. Expo.*, 2020, pp. 85–90.
[37] Y. Che, J. Xu, Y. Yang, J. Zhou, and Y. Zhao, "Large signal modeling method for AC/DC independent power system in DQ-coordinates," *IEEE Access*, vol. 6, pp. 32207–32215, 2018.
[38] S. Sen, P. L. Evans, and C. M. Johnson, "Multi-frequency averaging (MFA) model of electric-hybrid powertrain suitable for variable frequency operation applied in geographically-distributed power hardware-in-the-loop (GD-PHiL) simulation," in *Proc. IEEE Veh. Power Propulsion Conf.*, 2018, pp. 1–6.
[39] S. Sen, P. L. Evans, and C. M. Johnson, "Multi-frequency averaging (MFA) model of a generic electric vehicle powertrain suitable under variable frequency of averaging developed for remote operability," *IET Elect. Syst. Transp.*, vol. 10, no. 3, pp. 268–274, 2020.
[40] K. J. P. Veeramraju and J. W. Kimball, "Multidimensional extensions to generalized averaged models for multi-frequency-excited dynamic systems," in *Proc. IEEE 22nd Workshop Control Model. Power Electron.*, 2021, pp. 1–8.
[41] A. V. Oppenheim, A. S. Willsky, and S. H. Nawab, *Signals & Systems*, 2nd ed., Englewood Cliffs, NJ, USA: Prentice-Hall, 1996.
[42] P. Shamsi, "Extended averaging method for power supply systems with multiple switching frequencies," in *Proc. IEEE Appl. Power Electron. Conf. Expo.*, 2014, pp. 2842–2846.
[43] K. J. P. Veeramraju and J. Kimball, "EGAMToolbox," Apr. 2023. Accessed: Dec. 27, 2023. [Online]. Available: https://github.com/KartikeyaVeeramraju/EGAMToolbox
[44] J. Xu, H. Qian, Y. Hu, S. Bian, and S. Xie, "Overview of SOGI-based single-phase phase-locked loops for grid synchronization under complex grid conditions," *IEEE Access*, vol. 9, pp. 39275–39291, 2021.

Kartikeya Jayadurga Prasad Veeramraju (Graduate Student Member, IEEE) received the B.Tech. degree in electrical and electronics engineering from Kakatiya University, Warangal, India, in 2017, the M.S. and Ph.D. degrees in electrical engineering from the Missouri University of Science and Technology, Rolla, MO, USA, in 2020 and 2023, respectively.

He was a Key Member with Missouri S&T Satellite Team, where he has developed power converters for satellites, where he was a Graduate Teaching Assistant teaching Power Systems and Electromechanics Laboratory courses to undergraduate students. Since August 2023, he has been a Senior Power Electronics Firmware Engineer of lunar energy in Mountain View, CA, USA. His research interests include the design, modeling, and embedded control of power converters, microgrids, EV chargers, and high-voltage aerospace power converters.

Jonathan W. Kimball (Senior Member, IEEE) received the B.S. degree in electrical and computer engineering from Carnegie Mellon University, Pittsburgh, PA, USA, in 1994, and the M.S. degree in electrical engineering and the Ph.D. degree in electrical and computer engineering from the University of Illinois at Urbana-Champaign, Champaign, IL, USA, in 1996 and 2007, respectively.

From 1996 to 1998, he was with Motorola, Phoenix, AZ, USA, where he was involved in designing insulated gate bipolar transistor modules for industrial applications. He then joined Baldor Electric, Fort Smith, AR, USA, where he designed industrial adjustable-speed drives ranging 1–150 hp. In 2003, he joined as a Research Engineer with the University of Illinois at Urbana-Champaign, where he became a Senior Research Engineer. In 2003, he cofounded SmartSpark Energy Systems, Inc., Champaign, where he was the Vice President of Engineering. In 2008, he joined the Missouri University of Science and Technology, Rolla, MO, USA, where he is currently the Fred W. Finley Distinguished Professor of electrical engineering and the Chair of the Department of Electrical and Computer Engineering.

Dr. Kimball is a Member of Eta Kappa Nu, Piscataway, NJ, USA, Tau Beta Pi, Knoxville, TN, USA, and Phi Kappa Phi, Baton Rouge, LA, USA. He is a Licensed Professional Engineer in Illinois, USA.